Journal of Chromatography A, 1218 (2011) 4698–4708

Contents lists available at ScienceDirect

Journal of Chromatography A

journal homepage: www.elsevier.com/locate/chroma

Protein adsorption and transport in dextran-modified ion-exchange media. II. Intraparticle uptake and column breakthrough

Brian D. Bowes, Abraham M. Lenhoff*

Department of Chemical Engineering, University of Delaware, Newark, DE 19716, USA

ARTICLE INFO

Article history:
Received 12 March 2011
Received in revised form 13 May 2011
Accepted 16 May 2011
Available online 25 May 2011

Keywords:
Ion exchange
Dextran-grafted agarose
Confocal microscopy
Dynamic binding capacity

ABSTRACT

Protein transport behavior was compared for the traditional SP Sepharose Fast Flow and the dextran-modified SP Sepharose XL and Capto S resins. Examination of the dynamic binding capacities (DBCs) revealed a fundamental difference in the balance between transport and equilibrium capacity limitations when comparing the two resin classes, as reflected by differences in the locations of the maximum DBCs as a function of salt. In order to quantitatively compare transport behavior, confocal microscopy and batch uptake experiments were used to obtain estimates of intraparticle protein diffusivities. For the traditional particle, such diffusivity estimates could be used to predict column breakthrough behavior accurately. However, for the dextran-modified media, neither the pore- nor the homogeneous-diffusion model was adequate, as experimental dynamic binding capacities were consistently lower than predicted. In examining the shapes of breakthrough curves, it was apparent that the model predictions failed to capture two features observed for the dextran-modified media, but never seen for the traditional resin. Comparison of estimated effective pore diffusivities from confocal microscopy and batch uptake experiments revealed a discrepancy that led to the hypothesis that protein uptake in the dextran-modified resins could occur with a shrinking-core-like sharp uptake front, but with incomplete saturation. The reason for the incomplete saturation is speculated to be that protein initially fills the dextran layer with inefficient packing, but can rearrange over time to accommodate more protein. A conceptual model was developed to account for the partial shrinking-core uptake to test whether the physical intuition led to predictions consistent with experimental behavior. The model could correctly reproduce the two unique features of the breakthrough curves and, in sample applications, parameters found from the fit of one breakthrough curve could be used to adequately match breakthrough at a different flow rate or batch uptake behavior.

1. Introduction

Polymer-modified ion-exchange media are appealing for protein purification because of their high equilibrium and dynamic binding capacities. In previous work [1] we provided a brief review of the development and characterization of such media along with retention and equilibrium adsorption results for dextran-modified media. Column breakthrough behavior is an important factor in choosing a resin and reflects an interplay between protein adsorption and transport. Thus, the present work is aimed at complementing the insight into adsorption properties from the previous study with additional information about protein uptake.

Several previous studies have examined protein uptake behavior in polymer-modified media of various chemistries [2–8], including dextran-modified agarose resins [9–23]. Among these studies, quantitative information about uptake has been extracted both from bulk batch uptake experiments [19,20,23,24] and microscopic methods such as confocal laser scanning microscopy [11–15] or optical microscopy accounting for refractive index differences between protein-rich and protein-free regions [19,20,25,26]. Such studies have typically found rapid uptake in polymer-modified resins compared to that in traditional particles, with uptake of large proteins at low ionic strength being a notable exception [16]. A number of the studies on dextran-modified agarose have examined column breakthrough behavior with differing degrees of detail. Some report a few breakthrough curves or dynamic capacities [12,14,17,23] or report a small amount of detail for a large number of resins [9,10]. Others examine the effects of salt and pH on dynamic capacities more thoroughly [15,16], even including

* Corresponding author. Tel.: +1 302 831 8989; fax: +1 302 831 1048.
E-mail address: lenhoff@udel.edu (A.M. Lenhoff).

0021-9673/$ – see front matter © 2011 Elsevier B.V. All rights reserved.
doi:10.1016/j.chroma.2011.05.054

such ranges for multiple resins [22]. These studies have shown that maximum values of the DBC as a function of salt commonly exist because of slow intraparticle transport at low salt concentrations [15,16,22].

Relatively little information [18] has been presented on how well column behavior can be predicted from smaller-scale studies on polymer-modified resins. Intraparticle uptake of protein into chromatography media is often characterized by two limiting models: pore diffusion and homogeneous diffusion. In pore diffusion, only non-adsorbed protein is assumed to be free to diffuse, leading to the formation of a fairly sharp adsorption front. In the limit of a rectangular isotherm, shrinking-core behavior is encountered where the sharp front divides a protein-saturated outer shell and a protein-free inner core that shrinks with time. In homogeneous diffusion, even adsorbed protein is considered to be able to diffuse and a more diffuse intraparticle protein concentration profile is encountered.

In order to predict column breakthrough behavior, it is important to have an estimate of an appropriate diffusivity and it is helpful to also have some indication of the character of the intraparticle uptake. A macroscopic method, such as batch uptake, can generally be used to extract a diffusivity, but often cannot discriminate between pore- and homogeneous-diffusion behavior [24,27,28]. A microscopic method, such as confocal microscopy, can be used to distinguish between a radial distribution of protein within a particle that is sharp, consistent with pore-diffusion behavior under high-affinity binding conditions, or diffuse, consistent with homogeneous-diffusion behavior. However, estimating a diffusivity from confocal data is most straightforward when the uptake is consistent with pore diffusion [29] since there is no need to extract a protein concentration profile from intensity data corrected for light attenuation and dye reabsorption effects [30–33].

As in our previous work [1], the focus is on agarose-based media, employing the traditional SP Sepharose FF and the dextran-modified resins SP Sepharose XL and Capto S. Again, the role of protein size is examined, using the same model proteins to allow quantitative comparisons of equilibrium and dynamic capacities. The direct comparison of these capacities across a range of salt conditions is useful in understanding whether equilibrium or transport effects limit dynamic capacities. An additional important aspect of this work is in examining how well column breakthrough behavior can be predicted from smaller-scale studies and potential limitations of the traditional breakthrough models.

2. Materials and methods

2.1. Buffers, proteins, and resins

All buffers and protein solutions were prepared as described previously [1]. All experiments on lysozyme and lactoferrin were performed using pH 7 phosphate-buffered solutions while those on the mAb were performed in pH 5 acetate-buffered solutions. In preparing buffers at the desired ionic strengths, apparent pK_a values adjusted for solution conditions were used in place of thermodynamic pK_a values [34].

Cy5 fluorescent dye, purchased in prepacked vials (GE Healthcare, PA25001: Cy5 mono-reactive dye pack), was used in confocal microscopy studies. To label the proteins, a solution with roughly 20 mg/mL protein in 10 mM phosphate, pH 7 buffer or 10 mM acetate, pH 5 buffer was added to a vial of unreacted dye, which was then slowly rotated for 30 min. The protein–dye conjugate was recovered by visually collecting the first peak to elute from a 30 cm × 1.0 cm i.d. column gravity packed with Sephadex G-25 size-exclusion particles equilibrated in the desired buffer. The initial labeling resulted in an average of less than 0.3 dye molecules per protein molecule, suggesting that few protein molecules would have more than one label. Prior to use, labeled protein solutions were diluted with unlabeled protein to achieve a molar dye to protein ratio of 1:20 or less. The addition of a Cy5 dye molecule to a protein molecule results in a change in the protein net charge of −2, so the labeled protein isoforms should be somewhat less strongly retained than the native protein on cation exchange resins, as seems to be confirmed in experimental and theoretical studies of the effect [28,35–37].

The traditional resin SP Sepharose Fast Flow and the dextran-modified resins SP Sepharose XL and Capto S, all strong cation exchangers, were obtained from GE Healthcare. Since only the indicated SP or S versions of these resins were used in this work, they are referred to simply as FF, XL, and Capto, respectively. Pertinent properties of the resins were described previously [1].

2.2. Column breakthrough

Column breakthrough experiments were performed for each protein–resin pair on an ÄKTA Explorer 100 workstation (GE Healthcare). One low and one high superficial linear velocity (120 and 590 cm/h, respectively) were used to examine the effect of flow rate. For each combination of protein, resin, and flow rate, several ionic strengths were investigated with the particular aim of capturing a maximum DBC as function of total ionic strength (TIS), should one exist.

All column breakthrough experiments were performed using prepacked 2.5 cm × 0.7 cm i.d. HiTrap columns (GE Healthcare). Columns were first equilibrated with several column volumes of the desired buffer and then loaded via the sample pump on the ÄKTA with a solution of 2.00 ± 0.05 mg/mL protein in the same buffer. Loading continued until the protein concentration at the column outlet reached at least 60% of the feed concentration, as monitored by absorbance at 280 nm (A280). Protein was eluted using buffered solutions with 1 or 2 M NaCl. Mass balances for select runs confirmed that protein recovery was near 100%.

To determine DBC values accurately, one must subtract the system dead volume from experimental breakthrough curves. To determine this volume, a breakthrough curve was generated for the system with no column in place. On a plot of the ratio of the outlet and inlet protein concentrations (fractional breakthrough) as a function of volume fed, the system dead volume is the total area above the curve (and below unity), yielding an estimate of 1.1 mL. Experimental DBC values were determined by integrating the total area above breakthrough curves up to a cutoff of 10% breakthrough and subtracting the contribution due to the system dead volume.

2.3. Confocal microscopy imaging

Confocal laser scanning microscopy was used to monitor the transport of labeled protein in individual chromatography particles. The particles were packed in a flow cell designed for use with the confocal microscope, as has been described previously [29]. A multi-port valve (Omnifit, part 1126) was used to select between the equilibration buffer, protein solution, and elution buffer, with solvent flow being controlled by an LKB Bromma positive displacement pump. The feed protein concentration was 2.00 ± 0.05 mg/mL and, as in previous work [38], the flow rate of 1 mL/min was high enough to keep the particles stationary and to ensure that there was minimal depletion of protein in the flow cell volume of roughly 5 μL. A Zeiss 510 laser scanning microscope (Carl Zeiss, Germany) equipped with a 40× C-Apochromat (NA 1.2) water-immersion lens (Carl Zeiss) was used to visualize uptake.

The confocal microscopy experiments were used to gauge whether intraparticle uptake was qualitatively consistent with either pore- or homogeneous-diffusion behavior. No attempt was

made to extract diffusivities from data qualitatively consistent with homogeneous-diffusion behavior, but when the behavior appeared consistent with pore diffusion, an effective pore diffusivity was extracted based on the shrinking-core solution. Specifically, the diffusivity was determined by tracking η, which is the ratio of the radial position of the sharp front, R_f, and the particle radius, R_p. When depletion of protein from the bulk and external mass transfer resistance are negligible, the shrinking-core solution is given by [39]

$$\frac{D_e c_F}{{R_p}^2 q_{max}} t = I_2 - I_1 \quad (1)$$

where D_e is the effective pore diffusivity, c_F is the concentration of protein in the feed solution, q_{max} is the adsorbed phase concentration in equilibrium with c_F (taken as the plateau of the assumed rectangular isotherm), t is the time since uptake began, $I_1 = (\eta^2 - 1)/2$, and $I_2 = (\eta^3 - 1)/3$ [39].

2.4. Batch uptake

Batch uptake was performed in a manner similar to that used in numerous previous studies [4,5,27,29,32]. Briefly, 100 and 200 μL capillary tubes (Wiretrol II, Drummond Scientific) were used to add a known amount of particles to a protein solution in a 100 mL baffled beaker. An impeller was used to suspend the particles and mix the solution. The sample pump on the ÄKTA was used to withdraw the solution through a filter and pass it through the UV detector to monitor absorbance at 280 nm, returning the solution via an inlet at the base of the beaker. Batch uptake was only used to complement select confocal microscopy data.

Batch uptake experiments are notoriously poor at helping to discriminate between pore- and homogeneous-diffusion behavior, as both models tend to give good fits to batch uptake curves [24,27,28]. As such, a diffusivity can be estimated for either model to apply to prediction of breakthrough. For pore-diffusion behavior, if external mass transfer resistance is included, an estimate of the power input is needed to estimate the mass transfer coefficient. Using the correlation of Sano and Usui [40], a power input of 0.014 m^2/s^3 was estimated, comparable to the value of 0.045 m^2/s^3 found for the setup used by Weaver and Carta [4], though the exact value used has little influence on the final diffusivity estimate. Employing the correlation of Armenante and Kirwan [41], a value for the external mass transfer coefficient of $k_f = 1.4 \times 10^{-5}$ m/s was determined.

Inclusion of external mass transfer resistance in Eq. (1) gives

$$\frac{D_e c_F}{{R_p}^2 q_{max}} t = \left(1 - \frac{1}{Bi}\right) I_2 - I_1 \quad (2)$$

where $Bi = k_f R_p / D_e$ is the Biot number. Since protein depletion from the bulk is not negligible for batch uptake, the expressions for I_1 and I_2 become more complicated (see [28,39], for example, for details) and are not reproduced here. Eq. (2) is not easily rearranged to fit the adsorbed concentration, q, as a function of time, so I_2 was fitted using the nonlinear least-squares regression routine NLINFIT in Matlab.

For a homogeneous-diffusion fit, external mass transfer resistance is commonly ignored. Here, it is useful to work in terms of the fractional uptake, $F(t) = \bar{q}/q_{max}$, where the overline represents a concentration averaged over the particle volume. A useful approximation to the more rigorous infinite series solution was employed [5,42,43]:

$$F(t) = \left[1 - \exp\left(\pi^2 \left[-\tau + 0.960\tau^2 - 2.92\tau^3\right]\right)\right]^{1/2} \quad (3)$$

where $\tau = D_h t / {R_p}^2$ and D_h is the diffusivity for the homogeneous-diffusion model. In this case, a non-linear least squares fit was applied directly to the fractional uptake to extract an estimated diffusivity.

3. Results and discussion

3.1. Comparison of equilibrium and dynamic binding capacities

In the limit of an infinitely steep breakthrough curve, the DBC of a column will be equal to its equilibrium capacity. However, both intra- and extraparticle transport limitations give rise to breakthrough curves with finite slopes, meaning that the equilibrium capacity simply sets an upper bound on the DBC. Therefore, comparisons of equilibrium and dynamic capacities can provide insight into whether transport or equilibrium effects are limiting the DBC.

The most direct way to determine the equilibrium capacity of a column is to load protein onto the column until the fractional breakthrough reaches unity and then find the total area above the breakthrough curve. However, the protein requirements for such experiments can be prohibitive, so in this work, there were only two cases where the equilibrium capacity was estimated directly from column experiments: lactoferrin on FF at 400 mM TIS and the mAb on FF at 150 mM TIS.

For other cases, the equilibrium capacities were estimated from adsorption isotherms. These estimates used significantly less protein, but may be less accurate since they require knowledge of the column void fraction, ϵ; an additional source of uncertainty is that the isotherm and column breakthrough experiments were performed with different resin lots. To estimate the equilibrium capacities, Langmuir isotherm fits were used to estimate the adsorbed phase protein concentrations in equilibrium with the column loading concentration of 2 mg/mL and these adsorbed concentrations were converted to a mass per column volume basis. Estimates of ϵ were based on the retention time of blue dextran injections, which yielded values of 0.31, 0.24, and 0.36 for the respective FF, XL, and Capto HiTrap columns.

The equilibrium and dynamic capacities determined in this work are shown in Fig. 1, where the data for lysozyme on FF have been adapted from those of Dziennik et al. [29,44]. The scale is the same in all cases to facilitate direct comparison between all protein–resin pairs.

One important feature of these plots is that, for all cases except for lysozyme on the two dextran-modified resins, there exists a maximum DBC as a function of TIS. In the descending portion of the DBC curves, the DBCs come close to matching the equilibrium capacities, especially for the highest salt conditions at the lower flow rate, indicating that intraparticle transport is rapid and that the DBCs are controlled mainly by the equilibrium capacities. At low salt, though, the DBCs can be significantly lower than the equilibrium capacities, indicating that intraparticle transport is limiting the DBC. Extraparticle transport limitations should be present throughout the range of salt conditions and do not have as important an effect as intraparticle limitations. Since the equilibrium capacities decrease with increasing salt for all cases, the regions of increasing DBCs must mean that the improvements in intraparticle transport with increased salt more than offset the concomitant losses in equilibrium capacity. To account for the transport improvements in the ascending region, it has been suggested that bound proteins could electrostatically hinder the uptake of additional protein and that this hindrance would dissipate with increasing salt [16,32,45]. This effect would be expected to be most pronounced when the TIS is low and the protein occupies a significant fraction of the pore cross section. However, two other

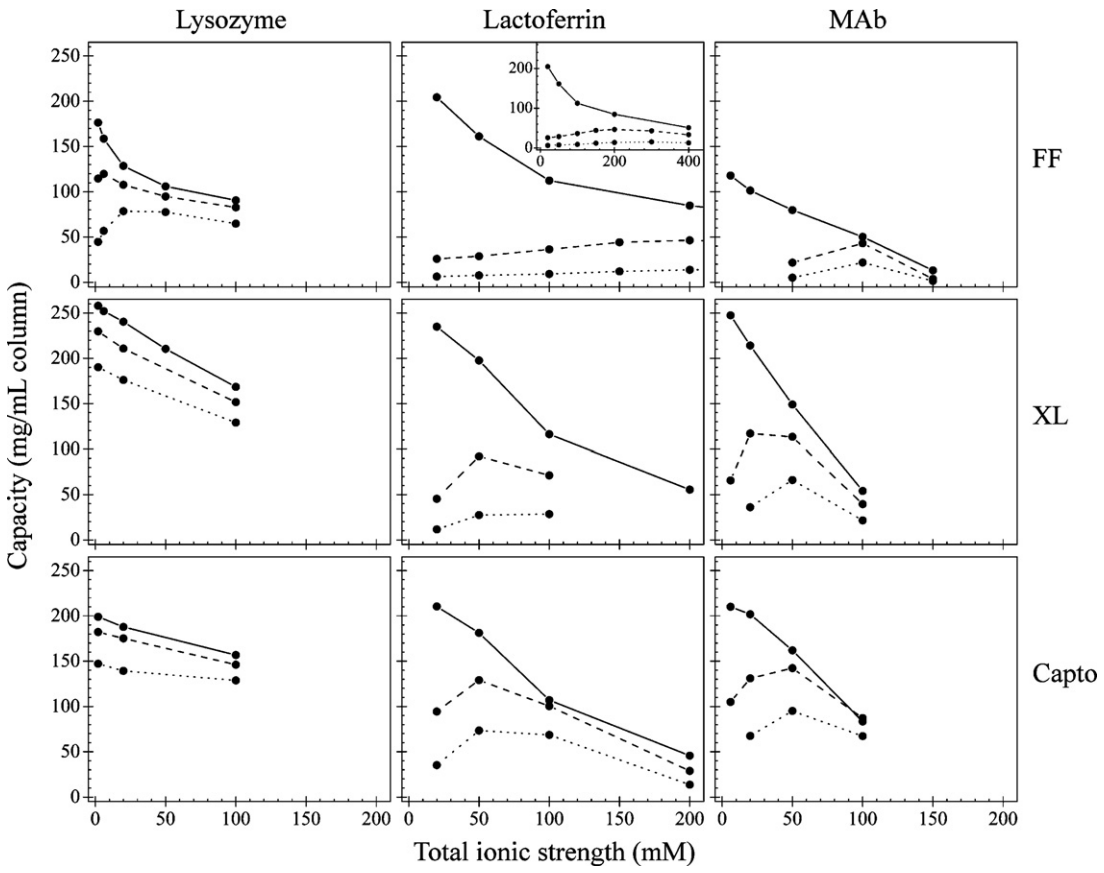

Fig. 1. Comparison of equilibrium column capacities (—) with dynamic binding capacities at 120 cm/h (– – –) and 590 cm/h (····). The inset for lactoferrin on FF shows the full range of data for that protein–resin pairing. All equilibrium capacities were estimated from adsorption isotherms with the exception of the capacities for lactoferrin on FF at 400 mM TIS and the mAb on FF at 150 mM TIS, which were determined directly from column loading experiments. A small discrepancy in the isotherm-estimated equilibrium capacity and the column-determined dynamic capacity is evident for the mAb on Capto at 100 mM TIS and is assumed to be due to use of different resin lots.

effects could account for the ascending portion of the DBC curves, even in the absence of electrostatic exclusion. First, if there exists parallel pore and surface [46] (or dextran-phase) diffusion, the increase in the latter with increased salt can give rise to significantly enhanced intraparticle transport [38]. Second, it is clear, especially from the lysozyme-FF data, that flow rate plays an important role [32,38] in determining the breadth or even the existence of the ascending region. This is because intraparticle transport resistance becomes relatively more important at higher flow rates, magnifying any differences in uptake rates at different salt concentrations. Thus, at sufficiently low flow rates the DBC should be primarily controlled by the equilibrium capacity rather than intraparticle uptake rates, decreasing monotonically with increasing salt. At higher flow rates the maximum DBC would shift downward and to a higher TIS where intraparticle uptake is faster, but the equilibrium capacity is lower.

Another important feature of the plots in Fig. 1 is the location of the maximum DBC when the three resins are compared for a given protein. For all three proteins, but most obviously for lactoferrin, the maximum DBC occurs at significantly lower TIS values for the two-dextran modified resins than for FF. It has been suggested that the salt concentration at which the maximum DBC occurs can be correlated to the net protein charge, independent of whether FF or XL is used [16], but the results in this work suggest that such a finding is not generally the case. Rather, the difference in the location of the maximum DBC as a function of TIS for the traditional and dextran-modified resins seems to reflect a fundamental difference in the balance between transport and adsorption. The finding of this fundamental difference motivates further investigation, especially with respect to equilibrium effects at high salt and transport effects at low salt.

3.2. Prediction of column breakthrough

3.2.1. Diffusivity estimates from confocal microscopy

In order to predict column breakthrough behavior, estimates for intraparticle diffusivities are needed. In this work, the primary method used to obtain diffusivities was through use of confocal microscopy data. As discussed previously, diffusivities are most easily obtained in cases where a sharp adsorption front, qualitatively consistent with shrinking-core behavior, is encountered. The combinations of protein, resin, and TIS that gave rise to such behavior are shown in Table 1 along with the corresponding estimates of the effective pore diffusivities. For lactoferrin on Capto and the mAb on XL at 50 mM TIS, estimates for the effective pore diffusivities approach the respective free solution diffusivities of 96 [47] and 47×10^{-12} m^2/s [48], indicating fast uptake. Another interesting trend is that the diffusivities for lactoferrin on XL are roughly constant between 50 and 200 mM TIS. Constant diffusivities as a function of salt are consistent with shrinking-core behavior. Sharp uptake profiles, qualitatively consistent with shrinking-core behavior, were required to fit the diffusivities from confocal microscopy images in the first place, so in the 50–200 mM TIS range, both the confocal images and the confocal-derived diffusivities seem consistent with shrinking-core behavior. The diffusivity is much lower at 20 mM TIS than in the 50–200 mM range, perhaps indicating that protein–protein repulsion significantly slows uptake only at this low-salt condition.

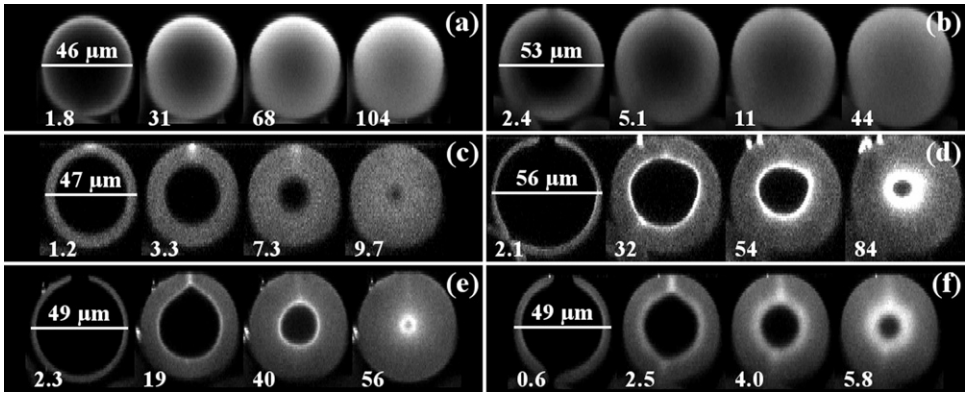

Fig. 2. Confocal microscopy images (x-z scans) of Cy5-labeled protein uptake. Top row: 20 mM TIS lysozyme uptake into (a) Capto and (b) XL at pH 7. Middle row: 20 mM TIS lactoferrin uptake into (c) Capto and (d) XL at pH 7. Bottom row: 50 mM mAb uptake into (e) FF and (f) XL at pH 5. Particle sizes are indicated by the scale bar in each panel and uptake times in minutes are indicated for each image. Gain settings vary between images, so intensities are not appropriate indicators of adsorbed concentrations, even in relative terms.

Fig. 2 shows three of the important comparative observations from the confocal microscopy imaging. In the top row, it is apparent that lysozyme uptake on Capto is slower than on XL (Fig. 2a and b, respectively). In both cases, the uptake profile is diffuse. Shrinking-core behavior has been found in confocal experiments previously for lysozyme on FF at pH 7 [29,32], but was not encountered on the dextran-modified media in this work, even at an ionic strength as low as 2 mM (confocal experiments for lysozyme on FF were not repeated in this work). The finding of qualitatively different uptake patterns between the two resin classes is interesting given that the isocratic retention behavior is similar for the three resins examined here [1] and that previous work for several traditional resins suggested that the qualitative uptake pattern could be correlated with the isocratic retention factor [38]. Thus, that correlation does not seem appropriate for polymer-modified resins, giving additional support to the assertion that there is a fundamental difference in the balance between transport and adsorption in the two resin classes. Previous work has shown that more diffuse uptake profiles were typically encountered for the descending portions of curves showing DBCs as a function of salt [16]. Since DBCs in this work decrease across the entire salt range for lysozyme on XL and Capto (Fig. 1), it is not surprising that shrinking-core behavior was not encountered for these protein–resin pairs.

The lack of shrinking-core behavior on the dextran-modified resins is in contrast to optical microscopy observations for lysozyme uptake on a custom XL-like particle referred to as SP-T40. At similar conditions (pH 6.5 and roughly 23 mM TIS compared to pH 7 and 20 mM TIS used in this work), a rapidly moving sharp front was observed for uptake on this resin [20]. It may simply be that the SP-T40 is different enough from the commercial SP XL resin to make direct comparisons inappropriate [24]. However, since estimates of effective pore diffusivities on SP-T40 were commonly several times the free solution diffusivities [20,24], perhaps indicative of the presence of homogeneous or dextran-phase diffusion [24] that would not be expected to yield a sharp uptake front, it could be informative to see whether differences in observed uptake patterns would be seen between the optical microscopy technique used for the SP-T40 studies and confocal microscopy images for the same conditions.

Table 1
Effective pore diffusivities estimated for conditions where confocal microscopy experiments revealed a sharp uptake front.

Resin	Protein	TIS (mM)	Diffusivity ($\times 10^{-12}$ m^2/s)
FF	LF	20	0.72
		100	2.3
	MAb	50	1.8
XL	LF	20	3.7
		50	21
		100	22
		200	17
	MAb	20	3.9
		50	48
Capto	LF	20	26
		50	74
	MAb	20	33

In the middle row of Fig. 2 showing lactoferrin uptake, it is seen that uptake is now much faster on Capto than on XL (Fig. 2c and d, respectively) and Table 1 shows that the same is true for the mAb. This ordering for the larger proteins is opposite to that for lysozyme uptake on these resins. The switch could be due to the higher static capacity of XL for lysozyme in the descending portion of the DBC curves or differences in the backbone agarose material in the resins. Regardless of the cause of the switch, the behavior is consistent with XL having the highest global DBC value for lysozyme, while Capto has the highest values for lactoferrin and the mAb (Fig. 1).

Uptake was consistently faster on the dextran-modified media than on FF and the bottom row of Fig. 2 shows the difference for uptake of the mAb on FF and XL (Fig. 2e and f, respectively). Both of these image sets, along with that for lactoferrin uptake on XL (Fig. 2d), show the much-debated overshoot ring at the uptake front (see [38], for example, for discussion). In this work, it is assumed that the overshoot is present due to displacement of the more weakly binding labeled protein by the more abundant unlabeled protein [28]. In this case, the sharp front indicates the dominance of pore diffusion and the movement of the front position over time should still allow for an estimate of the effective pore diffusivity. In all cases where the position of the sharp front is used to estimate the diffusivity, the estimate is expected to be an upper bound on the diffusivity. The upper bound is expected since the front for the more strongly bound native protein could lag behind the front for the observable mixture of labeled protein isoforms of lower net charge. However, previous comparisons of effective pore diffusivities obtained from batch experiments using native lysozyme and confocal experiments with Cy5-labeled lysozyme on FF found minimal differences for estimates from the two techniques [29,32]. Thus, the effect of labeling on estimated diffusivities is unlikely to be significant and seems to be relatively insensitive to the retention differences between native lysozyme and the isoforms of Cy5-labeled lysozyme that have been observed in work [37] where no

comparisons of batch- and confocal-determined diffusivities were made.

3.2.2. Comparison of experimental and predicted column breakthrough results

The diffusivity estimates, along with column and isotherm information, were used to make predictions of column breakthrough using a general shrinking-core solution for column behavior [49–51]. The model neglects axial dispersion, as is commonly assumed for macromolecules [28]. External mass transfer limitations were incorporated, with the mass transfer coefficient estimated using the correlation of Carberry [52]:

$$k_f = \frac{1.15D^{2/3}}{\left(2R_p/u\right)^{1/2}\nu^{1/6}} \quad (4)$$

where D is the free-solution diffusivity of the protein, u is the interstitial fluid linear velocity, and ν is the kinematic viscosity, taken to be 10^{-6} m^2/s.

Experimental results and predictions based on effective pore diffusivities obtained for lactoferrin from confocal microscopy experiments are shown in Fig. 3. With a system dead volume of roughly the same magnitude as the column volume, some deviation from an ideal step input of protein occurs experimentally, which will affect early-time behavior in the column. However, no attempt was made to account for this nonideality in the predictions, so it is expected that the initial portion of the predicted breakthrough curves will be sharper than would be observed experimentally. For the traditional FF particle (Fig. 3a), the model predictions capture the experimental behavior quite well, which suggests that the confocal-derived diffusivity estimates for lactoferrin are reasonable and are not significantly affected by labeling. However, for both XL and Capto (Fig. 3b and c, respectively), it is apparent that the model predictions are not nearly as accurate as for FF, especially at the lower ionic strengths. The disagreement at low ionic strength seems to be due to experimental breakthrough curves that start relatively steep, but then bend over much earlier than predicted, suggesting a slow approach to equilibrium. The slow equilibration could be indicative of a rearrangement process of adsorbed protein within the dextran layer, as protein gradually transitions from an initially inefficient packing to its maximum packing over time. The influence of the initially inefficient packing would be expected to be more severe when binding is tighter and adsorption is higher, i.e. at lower ionic strengths, as both of these factors would be expected to increase the steric barrier to additional adsorption within the dextran layer, necessitating longer times to reach maximum packing efficiency. Such a process would presumably be more severe in the three-dimensional dextran layer than on the two-dimensional agarose surface of FF, explaining why predictions are poor for the dextran-modified resins, but not for FF.

To further investigate the disagreement between experimental and predicted results for the dextran-modified media, a batch uptake experiment was run for 50 mM TIS lactoferrin uptake on XL. Estimated diffusivities of $D_e = 5.4 \times 10^{-12}$ m^2/s and $D_h = 5.9 \times 10^{-14}$ m^2/s were obtained for the shrinking-core and homogeneous-diffusion fits, respectively, and, not surprisingly considering previous work [24,27,28], both models gave good fits to the experimental data, as is evident in Fig. 4. This shrinking-core diffusivity estimate is roughly 4-fold lower than that obtained from confocal experiments, suggesting a problem with the applicability of the model, in spite of the sharp front observed in confocal imaging. Interestingly, such discrepancies were not observed for multiple batch versus optical microscopy comparisons in a study on custom-made XL-like particles [20]. However, given the much more rapid uptake observed on such particles compared to that on the commercial XL resin [24], conditions yielding significantly tighter binding may have been necessary to observe discrepancies for the custom particles, considering the trends in Fig. 3 for XL and Capto.

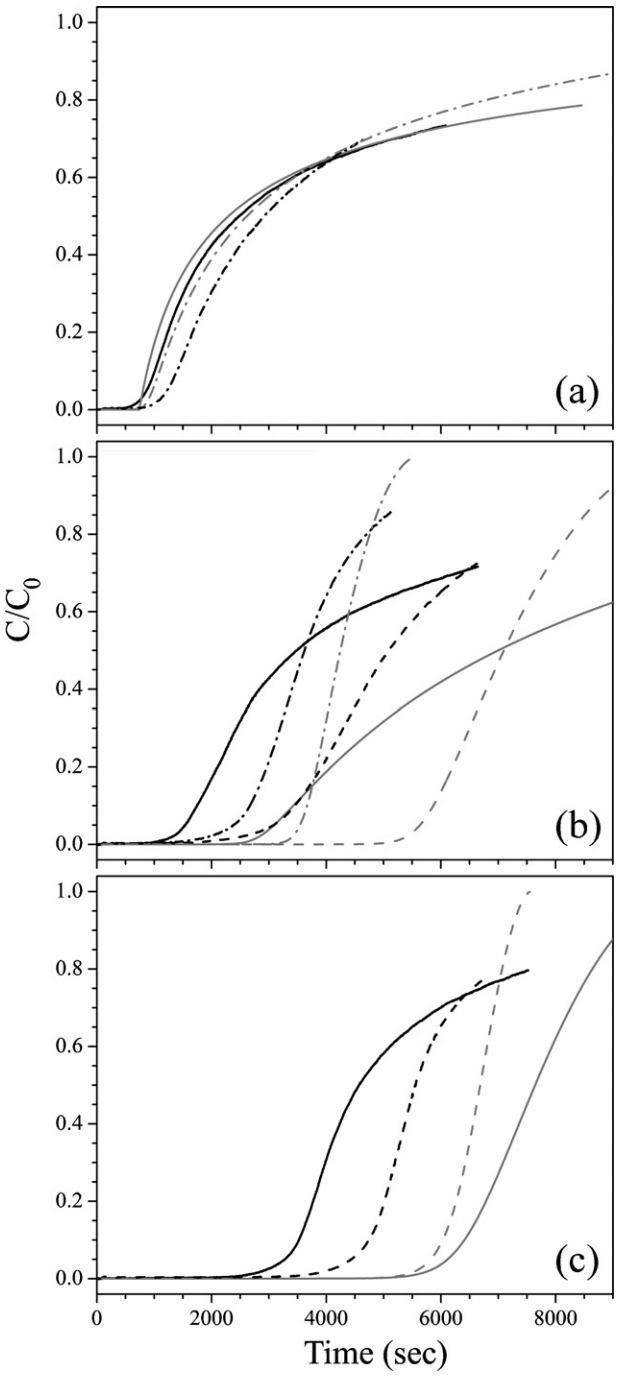

Fig. 3. Comparison of experimental (black) and predicted (gray) breakthrough curves for 2 mg/mL lactoferrin loading on (a) FF, (b) XL, and (c) Capto at 120 cm/h. Data are at total ionic strengths of 20 (—), 50 (– – –), and 100 mM (– · – · –).

Comparisons of the experimental breakthrough curves for lactoferrin at 50 mM TIS on XL with the various predictions are shown in Fig. 5, where the solution of Yoshida et al. [53] has been applied for the homogeneous diffusion case. Predictions based on the batch uptake data do not seem to resolve the issue of matching experimental data encountered with confocal microscopy data, though the shrinking-core fit from batch uptake at least gives a reasonable estimate of the DBC in this case. Since neither the batch- nor confocal-derived shrinking-core diffusivities give good fits to

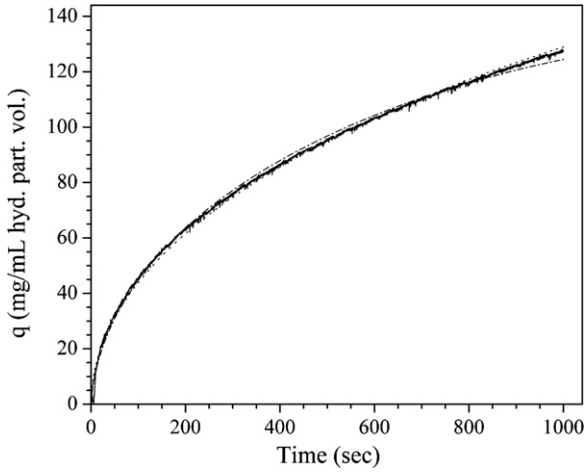

Fig. 4. Comparison of experimental (—), fitted, and predicted batch uptake curves for lactoferrin loading on XL at 50 mM TIS. Fitted curves for the pore- (– – –) and homogeneous-diffusion (· · · ·) models are shown along with the uptake curve for the partial shrinking-core model predicted from parameters found from fitting breakthrough curves (– · – · –).

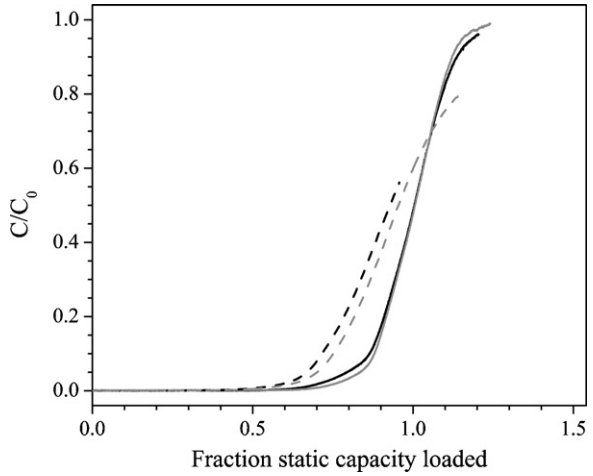

Fig. 6. Normalized breakthrough curves for 2 mg/mL lysozyme loading on XL at 2 (black) and 100 mM (gray) TIS and superficial linear velocities of 120 (—) and 590 cm/h (– – –).

the breakthrough curves, the 4-fold difference in these estimated diffusivities seems more likely to support the action of a slow rearrangement process of adsorbed protein (as already suggested by the slow equilibration in the breakthrough curves) than to indicate a problem with the confocal-derived diffusivities that is solely due to fluorescent labeling effects. The rearrangement process would cause the protein concentration to be less than its maximum value at the sharp front observed in confocal images and correction for the lower concentration would reduce the estimated diffusivity, bringing it closer to the value determined from batch uptake. Such rearrangement could also cause problems in determining a diffusivity using the previously mentioned [19,20,25,26] optical microscopy technique as accurate determination of the true uptake front position could be affected. For confocal images, correction for the rearrangement is perhaps more straightforward, as is addressed shortly.

Aside from the slow approach to equilibrium, a second feature observed in some experimental curves that is not captured by either of the traditional models is a pronounced kink in the early portion of the breakthrough curve. This behavior is visible, for example, in the data for lysozyme on XL in Fig. 6, especially at 120 cm/h. At this linear velocity, the initial breakthrough is gradual, but then increases sharply starting at roughly 85% of the static capacity. Such a kink could occur when column channeling is present, but symmetric acetone peaks seem to preclude that possibility in this work. Furthermore, the kinked behavior was observed only for the polymer-modified resins, not for FF, suggesting the behavior is unique to the polymer-modified resins. The behavior of the lysozyme-XL data is also interesting in that the curves at 2 and 100 mM TIS, plotted as a fraction of the static capacity loaded, collapse onto each other. The overlap suggests that transport is relatively similar at the two salt concentrations and could be useful for prediction of breakthrough at other salt conditions. However, this overlap of normalized curves only appeared for the small protein lysozyme on the dextran-modified media, so care would be required to verify the applicability of such predictions. Presumably, being in the descending portion of the DBC curves (Fig. 1) is necessary but not sufficient for such overlap.

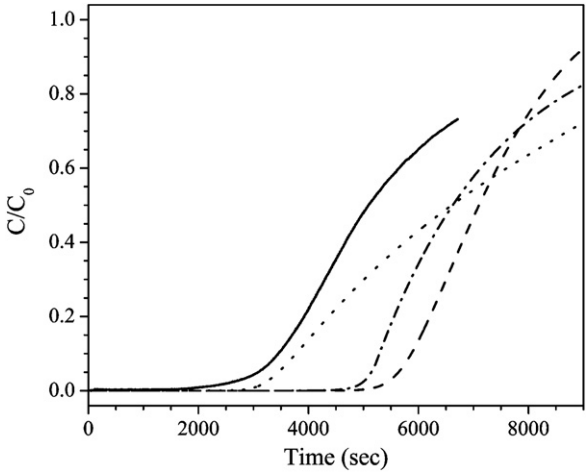

Fig. 5. Comparison of experimental (—) and predicted breakthrough curves for 2 mg/mL lactoferrin loading on XL at 120 cm/h and 50 mM TIS. Predictions are based on effective pore-diffusion coefficients from confocal (– – –) and batch uptake (· · · ·) experiments and a homogeneous-diffusion coefficient from batch uptake (– · – · –).

3.3. Model of uptake into dextran-modified media

An alternative model is sought to describe conditions where the traditional shrinking-core and homogeneous-diffusion models can accurately fit batch uptake results for the dextran-modified materials while failing to capture the correct column behavior. The key effect that we hypothesize to be lacking from the traditional models is the slow rearrangement of protein within the dextran layer that is assumed to be the cause of the observed slow approach to high equilibrium capacities. For the case where a sharp uptake front is observed in confocal microscopy, seemingly consistent with shrinking-core behavior, but with a slow approach to equilibrium that suggests true shrinking-core behavior does not exist, the behavior is referred to here as partial shrinking-core behavior. Schematically, the differences between true shrinking-core and the proposed partial shrinking-core behaviors are illustrated in Fig. 7. The protein uptake front is shown as being in the same position for the two models at each of the three time points, but the protein concentration and distribution are different. For the true shrinking-core process, as the front progresses, the protein concentration is at its maximum value at the position of the front and everywhere behind it. In contrast, in the partial shrinking-core description, the concentration at the front is only a fraction of the maximum concentration due to inefficient packing, as the protein has essentially reached a temporary jamming fraction. In this description,

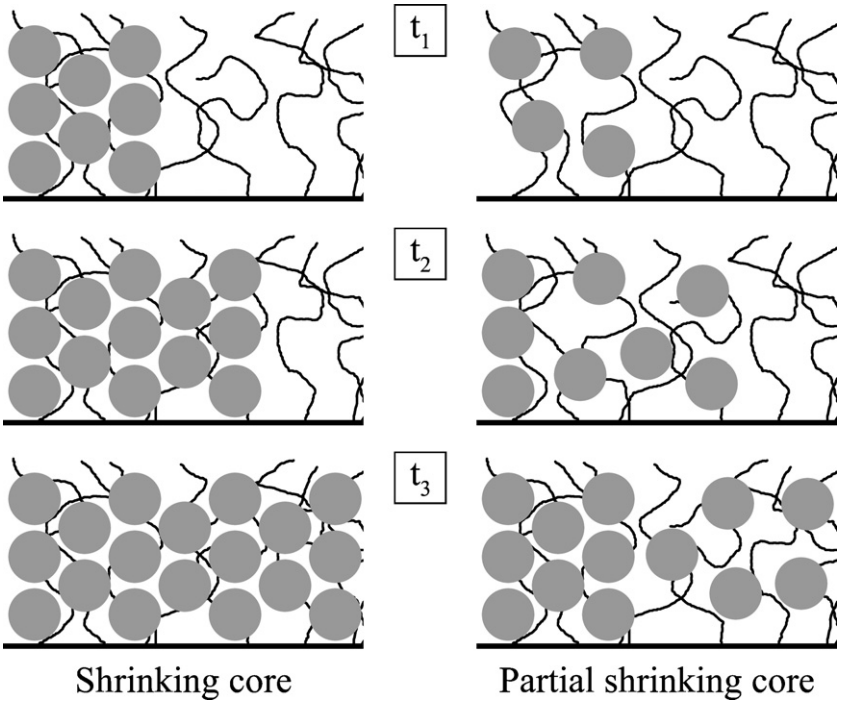

Fig. 7. Schematic representation of the differences in uptake progress over time for shrinking-core behavior (left side) and partial shrinking-core behavior (right side). In each panel, the thick black line at the bottom represents the agarose backbone, the thinner curved black lines represent the dextran extenders, and the gray circles represent protein molecules. At the progressive time points, $t_1 - t_3$, the front positions are the same for the two types of behavior. No information about the vertical distribution of protein within the dextran layer is meant to be implied for the partial shrinking-core behavior from the schematic representations.

the adsorbed concentration gradually fills in to the maximum value behind the front, though, as protein rearranges to pack more efficiently.

While steric effects on breakthrough curve shape have been considered based on random sequential adsorption on flat surfaces [54], adaptation to adsorption within the three-dimensional dextran layer would not be straightforward. Therefore, since neither the physical phenomena involved nor a mathematical description of the proposed rearrangement process is known, this model is only a conceptual one to assess whether the hypothesis yields predictions that are consistent with experimental observations.

3.3.1. Partial shrinking-core model development

In the conceptual model, uptake is assumed to comprise two processes. The first is shrinking-core uptake, but where the adsorbed amount, q_{sc}, reaches a maximum value, $q_{sc,max}$, that is only a fraction of the total capacity, q_{max}. This process is used to account for the observation that a sharp uptake front is observed in confocal experiments, seemingly consistent with the shrinking-core description, while acknowledging that the particles have not necessarily fully equilibrated during the shrinking-core process. In this process, the effective diffusivity, $D_{e,sc}$, is taken as the apparent diffusivity found from confocal experiments, $D_{e,app}$, scaled by the fraction $q_{sc,max}/q_{max}$ to account for the incomplete saturation. The second process accounts for the remaining adsorption, q_r, by employing a linear driving force (LDF) with a maximum difference $q_{r,max} = q_{max} - q_{sc,max}$ to account for the slow approach to equilibrium. This equilibration is assumed to be slow enough that the transport resistance is negligible. The simple LDF considers only an average particle concentration, so intraparticle concentration profiles cannot be generated from this model to compare with the schematic representation in Fig. 7.

Several dimensionless variables and parameters are defined:

$$\bar{Y}_{sc} = \frac{\bar{q}_{sc}}{q_{max}} \qquad \bar{Y}_r = \frac{\bar{q}_r}{q_{max}} \qquad \bar{X} = \frac{c_b}{c_F} \qquad \gamma = \frac{D_{e,sc}L}{{R_p}^2 u}$$
$$Bi = \frac{k_f R_p}{D_{e,sc}} \qquad St = \frac{k_r L}{u} \qquad \zeta = \frac{z}{L} \qquad \tau = \frac{ut}{L}$$

where $\bar{q}_i$ represents an adsorbed amount averaged over the particle volume, c_b is the concentration in the extraparticle fluid, L is the column length, u is the interstitial fluid linear velocity, k_f is the external mass transfer coefficient, k_r is the rate constant for the linear driving force, and z is the axial dimension of the column. Since the LDF is supposed to account for filling in behind the intraparticle shrinking-core front, we introduce a parameter, η_{start}, that indicates how far the shrinking-core front must progress into the particle before the LDF portion of uptake begins. That is, if we want the LDF to begin when the shrinking-core front has progressed one quarter of the radius into the particle, then $\eta_{start} = 0.75$. Alternatively, we can dictate the start of the LDF uptake by using the fraction of the shrinking-core portion of the capacity filled in using the relation

$$1 - {\eta_{start}}^3 = \frac{\bar{q}_{sc,start}}{q_{sc,max}} = \frac{\bar{Y}_{sc,start}}{Y_{sc,max}} \tag{5}$$

If axial dispersion is neglected, the dimensionless balance equations are

$$\frac{\partial \bar{X}}{\partial \zeta} + \frac{\partial \bar{X}}{\partial \tau} + \frac{1-\epsilon}{\epsilon}\frac{q_{max}}{c_F}\frac{\partial \bar{Y}}{\partial \tau} = 0 \tag{6a}$$

$$\frac{\partial \bar{Y}}{\partial \tau} = \frac{\partial \bar{Y}_{sc}}{\partial \tau} + \frac{\partial \bar{Y}_r}{\partial \tau} \tag{6b}$$

$$\frac{\partial \bar{Y}_{sc}}{\partial \tau} = 3\gamma \frac{c_F}{q_{max}} \frac{\bar{X}}{[(1-(\bar{Y}_{sc}/Y_{sc,max}))^{-1/3} - (1-(1/Bi))]} \tag{6c}$$

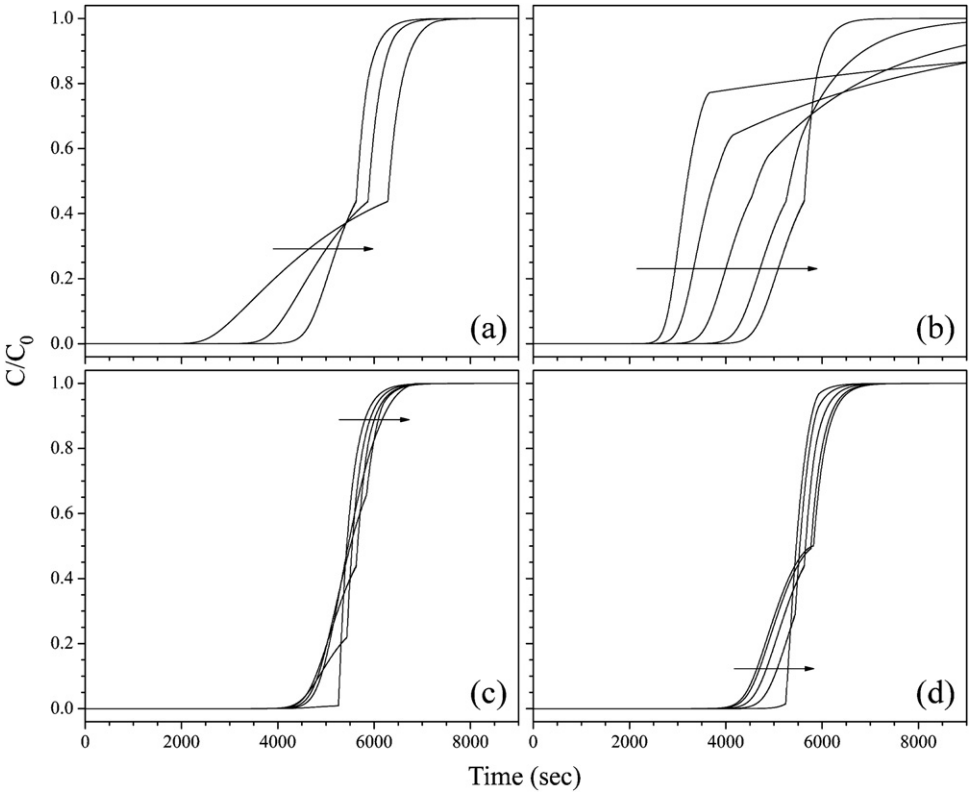

Fig. 8. Effects of parameters on predicted breakthrough curves from the partial shrinking-core model. Curves are for 2 mg/mL lactoferrin loading at 120 cm/h on the HiTrap XL column. A hypothetical Langmuir isotherm with parameters $q_m = 200$ mg/mL and $K = 10^5$ mL/mg, which is nearly rectangular, was employed along with an external mass transfer coefficient of $k_f = 1 \times 10^{-5}$ m/s. Base values for the varied parameters were $\eta_{start} = q_{sc,max}/q_{max} = 0.5$, $D_{e,sc} = 5 \times 10^{-11}$ m^2/s, and $k_r = 40 \times 10^{-4}$ s^{-1}. Effects of varied parameters are shown, with arrows indicating the direction of increasing value, in (a) with $D_{e,sc}$ values of 1, 2, and 5×10^{-11} m^2/s; (b) with k_r values of 1, 2, 4, 10, and 40×10^{-4} s^{-1}; (c) with $q_{sc,max}/q_{max}$ values of 0.01, 0.25, 0.50, 0.75, and 0.99; and (d) with η_{start} values of 0.01, 0.25, 0.50, 0.75, and 0.99. In each case, only one parameter is varied with remaining parameters fixed at the base values.

$$\bar{Y}_{sc} < \bar{Y}_{sc,start}: \quad \frac{\partial \bar{Y}_r}{\partial \tau} = 0$$
$$\bar{Y}_{sc} \geq \bar{Y}_{sc,start}: \quad \frac{\partial \bar{Y}_r}{\partial \tau} = St(Y_{r,iso} - \bar{Y}_r) \tag{6d}$$

where $Y_{r,iso} = q_{r,iso}/q_{max}$ and $q_{r,iso}$ is the adsorbed concentration in equilibrium with the local liquid phase concentration, obtainable from a Langmuir fit to isotherm data, for example. If $q_{sc,max} = q_{max}$, the model, of course, collapses to the traditional shrinking-core solution and an analytical solution is available [49–51]. For $q_{sc,max} < q_{max}$, an analytical solution is not available, so the model must be solved numerically. In this work, the forward-backward finite difference method [55,56] was used and gave an acceptable approximation to the analytical shrinking-core solution for $q_{sc,max} = q_{max}$.

For batch uptake behavior, it is often simpler to work in dimensional terms and the following balance equations apply:

$$\frac{dc_b}{dt} = \left(\frac{d\bar{q}_{sc}}{dt} + \frac{d\bar{q}_r}{dt}\right)\frac{V_{part}}{V_{liq}} \tag{7a}$$

$$\frac{d\bar{q}_{sc}}{dt} = \frac{3D_{e,sc}}{{R_p}^2}\frac{c_b}{[(1-(\bar{q}_{sc}/q_{sc,max}))^{-1/3} - (1-(1/Bi))]} \tag{7b}$$

$$\bar{q}_{sc} < \bar{q}_{sc,start}: \quad \frac{d\bar{q}_r}{dt} = 0$$
$$\bar{q}_{sc} \geq \bar{q}_{sc,start}: \quad \frac{d\bar{q}_r}{dt} = k_r\left(q_{r,iso} - \bar{q}_r\right) \tag{7c}$$

where V_{part} and V_{liq} are the hydrated particle and liquid volumes, respectively. Solute accumulation in the pore fluid is considered to be negligible in writing Eq. (7a). In this work, these equations were solved using the ODE45 function in Matlab.

3.3.2. Model features

The effects on output behavior of some of the most important parameters are shown in Fig. 8. Several aspects of the effects seen are relevant to the experimental breakthrough data. For example, Fig. 8a shows that the value of $D_{e,sc}$ primarily affects the steepness of the initial portion of breakthrough, with little effect on the shape of the latter portion of the curve. From Fig. 8b it is apparent that low values of the parameter k_r qualitatively capture the steep initial breakthrough followed by a slow approach to equilibrium seen for low-salt breakthrough on XL and Capto (Fig. 3) and the resulting loss of DBC. Also, it can be seen that either a low value of $q_{sc,max}/q_{max}$ or a high value of η_{start} (Fig. 8c and d, respectively) gives rise to a pronounced kink in the early portion of the breakthrough curves such as that observed in Fig. 6. In fact, such a kink is observed for most of the predicted curves. In the case where the kink leads to a steeper slope, the kink reflects the time when the LDF portion of uptake starts to occur at the column outlet. From Fig. 8b one can see that, as the value of k_r decreases, this type of kink dies out and, when k_r is low enough, a kink followed by a region of decreased slope appears. This latter kink reflects a case where the shrinking-core portion of uptake is complete and the remaining capacity is being filled exclusively by the LDF. In practice, of course, neither type of kink would be as sharp as predicted, for two obvious reasons. First, in the model, the LDF is artificially either on or off, but realistically, resistance to the remaining uptake behind the sharp front would be expected to gradually phase in over time. Second,

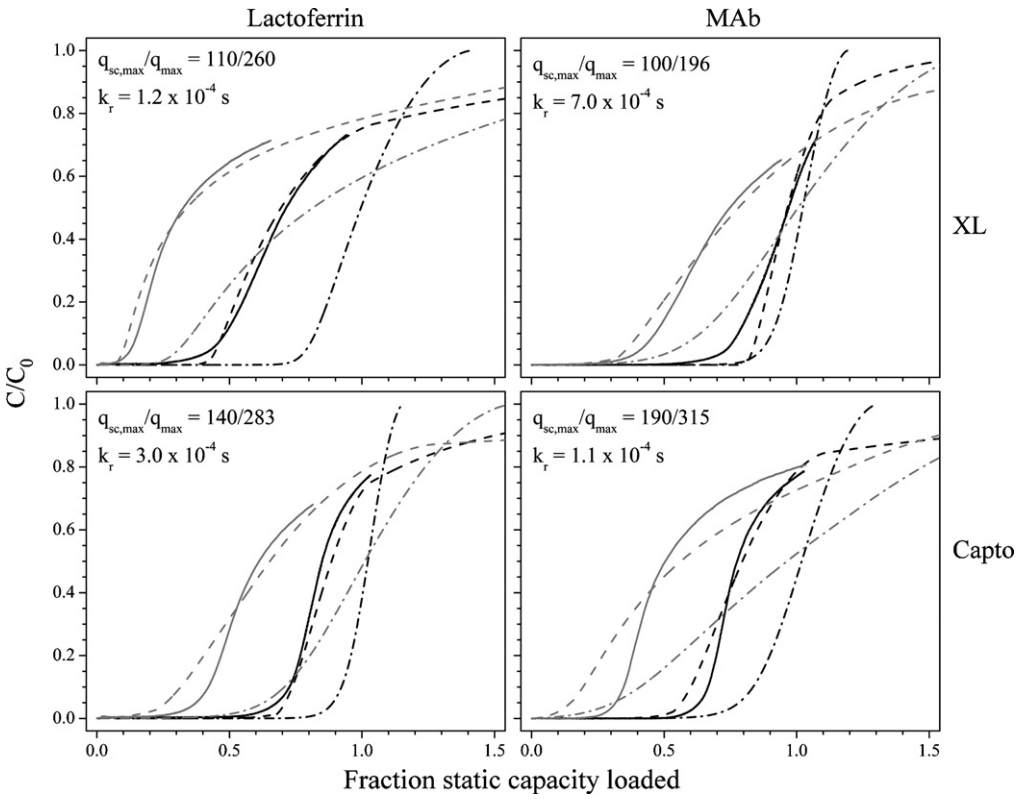

Fig. 9. Comparison of experimental column breakthrough curves (—) and curves predicted from the partial shrinking-core (– – –) and traditional shrinking-core (– · – ·) models. Data are for 2 mg/mL loading at 120 cm/h (black) and 590 cm/h (gray) for the indicated protein–resin pairs. All data are at 50 mM TIS, with the exception of the mAb on Capto, which is at 20 mM TIS. Parameters used for the partial shrinking-core model are listed in each panel.

accounting for the distribution of resin particle sizes would help to smooth the transition behavior. Nonetheless, the model does seem to correctly exhibit the two distinctive features observed for some breakthrough data on polymer-modified media: a slow approach to equilibrium and a pronounced kink.

3.3.3. Model application

To test the direct application of the conceptual model to experimental data, the model was applied to four sets of breakthrough curves. Because the conceptual model has three independent parameters not present in the traditional shrinking-core model, direct fitting of the model to breakthrough curves is not an adequate test of its success. However, in the absence of independent methods for estimating the parameters, we combine approximate parameter estimation with tests to assess the effectiveness of those parameters at predicting behavior under different conditions. In each case, the model curve was visually fit to the experimental breakthrough curve for 2 mg/mL loading at 120 cm/h using the two adjustable parameters $q_{sc,max}$ and k_r. Since $1/k_r$ represents a characteristic time scale for the slow approach to equilibrium, a reasonable approximation of k_r can be estimated a priori based on an experimental breakthrough curve. For η_{start}, as with k_r, there is some physical basis for its selection. For a large protein under strong binding conditions, η_{start} should approach unity and should be coupled with a low k_r value, indicating that a strong resistance to additional uptake begins almost immediately after the shrinking core front enters a particle at a given axial position. A smaller value of η_{start} combined with a higher k_r value would be appropriate for weaker binding or a smaller protein since adsorption in the outer shell of a particle would have less of an effect on additional uptake than for a large, tightly bound protein. Based on this rationale, a high value of η_{start} = 0.99 was chosen for the breakthrough curves considered here. Evidence for lower values of η_{start} will be presented elsewhere and may also exist in the data of Franke et al. [57] for the polymer-modified resin Fractogel EMD SO_3^-. Remaining inputs were available from isotherm and confocal microscopy experiments, column geometry, and the correlation for the external mass transfer coefficient.

Comparisons of the experimental and predicted breakthrough curves for the four test sets are shown in Fig. 9. In each panel, the experimental curves at 120 and 590 cm/h are shown along with the curves predicted from the partial shrinking-core and traditional shrinking-core models. In all cases, the visually fit partial shrinking-core curve better matches the 120 cm/h data than the traditional shrinking-core prediction. However, this only serves to show that the model can correctly capture the shape of experimental data and gives no indication of quantitative utility. For the fitted parameters to be meaningful, they should also apply at the higher superficial linear velocity of 590 cm/h, with only the value of the external mass transfer coefficient changing. From Fig. 9, it is clear that the fits at 590 cm/h using the parameters from the 120 cm/h fit are not as good as for the original 120 cm/h fits, but still remain better than the traditional shrinking-core predictions. The 590 cm/h fit is least good for the mAb on Capto. This may be because these data are at the lowest ionic strength, where protein–protein repulsion would presumably have the most pronounced effect on uptake. Thus, the partial shrinking-core model may be best suited to moderate salt conditions.

As an additional test, the parameters from breakthrough data must give a predicted batch uptake curve that is consistent with experimental behavior. Experimental data for lactoferrin uptake on XL at 50 mM TIS were used for such a comparison. Fig. 4 shows the experimental uptake curve, the fitted curves based on the estimated diffusivities from Section 3.2.2, and the curve predicted from the partial shrinking-core model fit to the 120 cm/h breakthrough data (upper left panel in Fig. 9). As was mentioned

previously, the shrinking-core and homogeneous-diffusion fits, not surprisingly, nicely match the experimental data, but the fit for the partial shrinking-core prediction is also good, confirming consistency across experiments for the single set of estimated parameters. This consistency seems to make it unlikely that the success of the original fit to the 120 cm/h breakthrough data is solely a consequence of the extra parameters in the model, but rather seems to confirm that the physical intuition used to develop the model is reasonable.

4. Conclusions

This work has combined adsorption and transport information to examine trends in column breakthrough behavior. In particular, comparison of the equilibrium and dynamic binding capacities across a range of salt conditions proved useful for understanding whether equilibrium or kinetic effects were limiting and could provide guidance as to how improvements in column loading performance might be realized. Such comparisons help to highlight some of the fundamental differences in the adsorption-transport interplay between the traditional and dextran-modified media.

Additionally, this work highlights some shortcomings in using the traditional shrinking-core and homogeneous-diffusion models for the prediction of column breakthrough behavior on dextran-modified media. Clearly, using diffusivities obtained from microscopic and batch methods with these models led to some poor predictions of column behavior, as the inclusion of the axial dimension in the column revealed discrepancies that were not apparent in model fits to the small-scale data. Such discrepancies suggest that diffusivities obtained in the absence of column experiments may provide an incomplete and perhaps even misleading description of uptake. This work sought to address the limitations found in the traditional models using physical intuition combined with experimental evidence to develop a conceptual model. This partial shrinking-core model seems to correctly capture some of the distinctive features observed for breakthrough on the dextran-modified media. However, work certainly remains to make the model more mechanistic and predictive. In the current form of the model, the traditional path of predicting column breakthrough behavior from batch uptake data is not feasible. This limitation exists because the traditional shrinking-core solution remains as a suitable fit to batch uptake data, leaving no way to estimate the fraction of uptake that should be apportioned to the shrinking-core and LDF aspects of the model. Presumably, implementation of a more mechanistic description of the slow approach to equilibrium would help overcome this limitation to allow breakthrough prediction from batch uptake or microscopically observed behavior rather than from other breakthrough data.

Acknowledgments

We thank DMV-International for donating the lactoferrin and Biogen Idec for donating the mAb. We also thank Kirk Czymmek and Jeffrey Caplan for guidance on the confocal microscopy imaging. We are grateful for financial support from the NSF (NSF IGERT program and grant CBET-0828590) and the NIH (grant R01 GM75047).

References

[1] B.D. Bowes, H. Koku, K.J. Czymmek, A.M. Lenhoff, J. Chromatogr. A 1216 (2009) 7774.
[2] E. Müller, Chem. Eng. Technol. 28 (2005) 1295.
[3] E. Boschetti, J.L. Coffman, G. Subramanian, Bioseparation and Bioprocessing, Wiley-VCH, New York, NY, 1998, p. 157.
[4] L.E. Weaver, G. Carta, Biotechnol. Prog. 12 (1996) 342.
[5] M.A. Fernandez, G. Carta, J. Chromatogr. A 746 (1996) 169.
[6] M.A. Fernandez, W.S. Laughinghouse, G. Carta, J. Chromatogr. A 746 (1996) 185.
[7] R.K. Lewus, F.H. Altan, G. Carta, Ind. Eng. Chem. Res. 37 (1998) 1079.
[8] M. Urmann, H. Graalfs, M. Joehnck, L.R. Jacob, C. Frech, mAbs 2 (2010) 395.
[9] A. Staby, I.H. Jensen, J. Chromatogr. A 908 (2001) 149.
[10] A. Staby, M.B. Sand, R.G. Hansen, J.H. Jacobsen, L.A. Andersen, M. Gerstenberg, U.K. Bruus, I.H. Jensen, J. Chromatogr. A 1034 (2004) 85.
[11] A. Ljunglöf, J. Thömmes, J. Chromatogr. A 813 (1998) 387.
[12] J. Hubbuch, T. Linden, E. Knieps, J. Thommes, M. Kula, Biotechnol. Bioeng. 80 (2002) 359.
[13] J. Hubbuch, T. Linden, E. Knieps, A. Ljunglöf, J. Thömmes, M.R. Kula, J. Chromatogr. A 1021 (2003) 93.
[14] J. Hubbuch, T. Linden, E. Knieps, J. Thömmes, M.R. Kula, J. Chromatogr. A 1021 (2003) 105.
[15] A. Ljunglöf, K.M. Lacki, J. Mueller, C. Harinarayan, R. van Reis, R. Fahrner, J.M. Van Alstine, Biotechnol. Bioeng. 96 (2007) 515.
[16] C. Harinarayan, J. Mueller, A. Ljunglöf, R. Fahrner, J. Van Alstine, R. van Reis, Biotechnol. Bioeng. 95 (2006) 775.
[17] N. Tugcu, D.J. Roush, K.E. Göklen, Biotechnol. Bioeng. 99 (2008) 599.
[18] T. Bergander, K. Nilsson-Vaelimaa, K. Oberg, K.M. Lacki, Biotechnol. Prog. 24 (2008) 632.
[19] Y. Tao, G. Carta, J. Chromatogr. A 1211 (2008) 70.
[20] M.C. Stone, Y. Tao, G. Carta, J. Chromatogr. A 1216 (2009) 4465.
[21] E.J. Suda, K.E. Thomas, T.M. Pabst, P. Mensah, N. Ramasubramanyan, M.E. Gustafson, A.K. Hunter, J. Chromatogr. A 1216 (2009) 5256.
[22] T.M. Pabst, E.J. Suda, K.E. Thomas, P. Mensah, N. Ramasubramanyan, M.E. Gustafson, A.K. Hunter, J. Chromatogr. A 1216 (2009) 7950.
[23] Q.H. Shi, G.D. Jia, Y. Sun, J. Chromatogr. A 1217 (2010) 5084.
[24] M.C. Stone, G. Carta, J. Chromatogr. A 1146 (2007) 202.
[25] M.C. Stone, G. Carta, J. Chromatogr. A 1160 (2007) 206.
[26] T.E. Bankston, M.C. Stone, G. Carta, J. Chromatogr. A 1188 (2008) 242.
[27] C. Chang, A.M. Lenhoff, J. Chromatogr. A 827 (1998) 281.
[28] G. Carta, A.R. Ubiera, T.M. Pabst, Chem. Eng. Technol. 28 (2005) 1252.
[29] S.R. Dziennik, E.B. Belcher, G.A. Barker, M.J. DeBergalis, S.E. Fernandez, A.M. Lenhoff, Proc. Natl. Acad. Sci. U. S. A. 100 (2003) 420.
[30] T.D. Visser, F.C.A. Groen, G.J. Brakenhoff, J. Microsc. -Oxf. 163 (1991) 189.
[31] J.B.T.M. Roerdink, M. Bakker, J. Microsc. -Oxf. 169 (1993) 3.
[32] S.R. Dziennik, E.B. Belcher, G.A. Barker, A.M. Lenhoff, Biotechnol. Bioeng. 91 (2005) 139.
[33] K. Yang, Q.H. Shi, Y. Sun, J. Chromatogr. A 1136 (2006) 19.
[34] R.J. Beynon, J.S. Easterby, Buffer Solutions, The Basics Series, IRL Press at Oxford University Press, New York, 1996.
[35] C. Teske, M. Schroeder, R. Simon, J. Hubbuch, J. Phys. Chem. B 109 (2005) 13811.
[36] C.A. Teske, E. von Lieres, M. Schroder, A. Ladiwala, S.M. Cramer, J.J. Hubbuch, Biotechnol. Bioeng. 95 (2006) 58.
[37] C.A. Teske, R. Simon, A. Niebisch, J. Hubbuch, Biotechnol. Bioeng. 98 (2007) 193.
[38] J.F. Langford, X. Xu, Y. Yao, S.F. Maloney, A.M. Lenhoff Jr., J. Chromatogr. A 1163 (2007) 190.
[39] W.K. Teo, D.M. Ruthven, Ind. Eng. Chem. Proc. Des. Dev. 25 (1986) 17.
[40] Y. Sano, H. Usui, J. Chem. Eng. Jpn. 18 (1985) 47.
[41] P.M. Armenante, D.J. Kirwan, Chem. Eng. Sci. 44 (1989) 2781.
[42] F. Helfferich, M.S. Plesset, J. Chem. Phys. 28 (1958) 418.
[43] F. Helfferich, J. Chem. Phys. 29 (1958) 679.
[44] S.R. Dziennik, Ph.D. dissertation, Department of Chemical Engineering, University of Delaware, Newark, DE (2002).
[45] A.L. Zydney, C. Harinarayan, R. van Reis, Biotechnol. Bioeng. 102 (2009) 1131.
[46] H. Yoshida, M. Yoshikawa, T. Kataoka, AIChE J. 40 (1994) 2034.
[47] B. Chaufer, M. Rabiller-Baudry, D. Lucas, F. Michel, M. Timmer, Lait 80 (2000) 197.
[48] M.E. Young, P.A. Carroad, R.L. Bell, Biotechnol. Bioeng. 22 (1980) 947.
[49] K.R. Hall, L.C. Eagleton, A. Acrivos, T. Vermeulen, Ind. Eng. Chem. 5 (1966) 212.
[50] R.S. Cooper, D.A. Liberman, Ind. Eng. Chem. 9 (1970) 620.
[51] T.W. Weber, R.K. Chakravorti, AIChE J. 20 (1974) 228.
[52] J.J. Carberry, AIChE J. 6 (1960) 460.
[53] H. Yoshida, T. Kataoka, D.M. Ruthven, Chem. Eng. Sci. 39 (1984) 1489.
[54] X.Z. Jin, J. Talbot, N.H.L. Wang, AICHE J. 40 (1994) 1685.
[55] M. Czok, G. Guiochon, Anal. Chem. 62 (1990) 189.
[56] G. Guiochon, Fundamentals of Prepartative and Nonlinear Chromatography, Academic Press, New York, 1994.
[57] A. Franke, N. Forrer, A. Butte, B. Cvijetic, M. Morbidelli, M. Joehnck, M. Schulte, J. Chromatogr. A 1217 (2010) 2216.